Electrical Power and Energy Systems 72 (2015) 3–15

Contents lists available at ScienceDirect

Electrical Power and Energy Systems

journal homepage: www.elsevier.com/locate/ijepes

Small-signal modeling and parametric sensitivity of a virtual synchronous machine in islanded operation

Salvatore D'Arco [a], Jon Are Suul [a,b,*], Olav B. Fosso [b]

[a] SINTEF Energy Research, 7465 Trondheim, Norway
[b] Department of Electric Power Engineering, Norwegian University of Science and Technology, 7495 Trondheim, Norway

ARTICLE INFO

Article history:
Received 1 February 2015
Accepted 16 February 2015
Available online 29 March 2015

Keywords:
Power electronic control
Small-signal stability
Stand-alone operation
Virtual synchronous machine

ABSTRACT

The concept of Virtual Synchronous Machines (VSMs) is emerging as a flexible approach for controlling power electronic converters in grid-connected as well as in stand-alone or microgrid applications. Several VSM implementations have been proposed, with the emulation of inertia and damping of a traditional Synchronous Machine (SM) as their common feature. This paper investigates a VSM implementation based on a Voltage Source Converter (VSC), where a virtual swing equation provides the phase orientation of cascaded voltage and current controllers in a synchronous reference frame. The control system also includes a virtual impedance and an outer loop frequency droop controller which is functionally equivalent to the governor of a traditional SM. The inherent capability of the investigated VSM implementation to operate in both grid-connected and islanded mode is demonstrated by numerical simulations. Then, a linearized small-signal model of the VSM operated in islanded mode while feeding a local load is developed and verified by comparing its dynamic response to the time-domain simulation of a nonlinear system model. Finally, this small-signal model is applied to identify the dominant modes of the system and to investigate their parametric sensitivity.

Introduction

Virtual Synchronous Machines (VSMs) have recently been proposed as a suitable concept for controlling power electronic converters in power system applications [1–4]. In the context of large-scale power systems, VSMs can provide a flexible approach for introducing additional damping and virtual inertia as an inherent part of the control system of grid integrated Voltage Source Converters (VSCs) [2,5,6]. A few proposed implementations of the VSM concept can also allow for stand-alone and parallel-connected operation in Microgrids or other isolated system configurations with similar performance and flexibility as traditional Synchronous Machines (SMs) [4,7–9].

The VSM concept is still in an early stage of development and many possible implementations, targeted for various types of applications, have been proposed, as reviewed in [4,10]. Thus, most publications until now have been mainly concerned with the development of particular VSM implementations and the presentation of case studies demonstrating the corresponding operational features. A systematic small-signal analysis of a specific VSM implementation was first presented in [11], intended for controller tuning and stability improvement by utilizing the sensitivities of the system eigenvalues with respect to the controller parameters.

The VSC control system investigated in [11] included only the VSM swing equation for damping and inertia emulation, a droop-based reactive power controller according to [12,13] and cascaded voltage and current control loops. However, there was no external power control included in the model, and the implementation of the damping of the VSM did not automatically take into account variations in the steady-state grid frequency. Thus, the applicability of the studied control system was limited to either stand-alone operation for feeding a local load or the operation in a strong grid with a known, fixed, frequency. An extension of the VSM control system design described in [11] was presented in [14]. To achieve full flexibility in allowable operating conditions, the resulting control system included an outer loop frequency droop controller with functionality equivalent to the steady-state control characteristics of traditional SMs [16]. A Phase Locked Loop (PLL) [17,18] was also introduced for tracking the actual grid frequency needed for implementing the VSM inertial damping under deviations from the nominal grid frequency. Furthermore, a virtual impedance, similar to the implementations proposed in [19,20], was included in the

* Corresponding author at: SINTEF Energy Research, Postboks 4761 Sluppen, 7465 Trondheim, Norway. Tel.: +47 95 91 09 13.
E-mail addresses: salvatore.darco@sintef.no (S. D'Arco), Jon.A.Suul@sintef.no, jon.are.suul@ntnu.no (J.A. Suul), olav.fosso@ntnu.no (O.B. Fosso).

http://dx.doi.org/10.1016/j.ijepes.2015.02.005
0142-0615/

VSM to improve the decoupling between active and reactive power when operating in resistive grids. Active damping of LC-oscillations was also introduced to ensure stable operation of the VSM in case of LC or LCL filters as the grid side interface of the VSC [21,22]. Mathematical models for all the individual elements of the investigated VSM configuration were described in detail in [14], and a corresponding small-signal state-space model of the entire system was developed, verified and analyzed for grid connected operation. The same control system and the corresponding small signal model for grid connected operation was further elaborated and analyzed in [15].

Although the mathematical model and the analysis of the VSM implementation from [14] and [15] were only valid for grid connected operation, the presented VSM implementation was also intrinsically suitable for stand-alone operation. This paper will start from the same control system implementation and the corresponding model description as presented in [14], and will demonstrate the inherent capability of this VSM implementation for both grid-connected and stand-alone operation by time-domain simulations. A nonlinear analytical model for stand-alone operation will be formulated and linearized to obtain a small-signal state-space representation. This model will be validated by simulations of the nonlinear system model and applied to study the small-signal dynamic properties of the VSM in islanded operation. In particular, the model will be used to analyze the influence of operating conditions on the VSM performance in stand-alone mode, and to identify the parametric sensitivity of the dominant eigenvalues. Together with the results presented in [14], this will provide a complete framework for analyzing the tuning and the dynamic operation of the investigated VSM implementation in both grid-connected and stand-alone operation.

Virtual synchronous machine modeling

This section presents the investigated VSM-based control scheme and the modeling of its functional elements. It is assumed that the dc-link of the VSC is connected to an energy storage unit or to a source with sufficient available buffer capacity. The dc voltage is assumed to be determined by this source, so the modeling and control of the dc side of the converter will not be further discussed. Although most parts of the model description are available in [14], all main equations and descriptions are repeated here for completeness of the presentation when introducing the adaptations required to represent the VSM in stand-alone operation.

System configuration and control system overview

An overview of the studied VSM configuration is shown in Fig. 1, where a VSC is connected to a grid or a local load through an LC filter. For simplicity in the modeling, the local load is connected in parallel to a stiff voltage source. Thus, the investigated system will represent grid connected operation when the breaker indicated in the figure is closed as discussed in [14], while it will represent stand-alone operation for feeding a local load when the breaker is open.

As indicated in Fig. 1, the VSM-based power control with virtual inertia provides frequency and phase angle references to the VSC control system while a reactive power controller provides the voltage amplitude reference. Thus, the VSM inertia and the reactive power controller appear as outer loops providing the references for the cascaded voltage and current controllers in a synchronously rotating reference frame. A PLL detects the actual grid frequency, but it should be noted that this frequency is only used for implementing the damping term of the VSM swing equation. Thus, the reference frame orientation of the inner loop controllers of the VSC is determined only by the power-balance-based synchronization mechanism of the VSM inertia and does not rely on the PLL as in conventional control systems. This applies both when grid connected and in stand-alone operation where the operating frequency of the VSM will be determined by the power balance of the VSM and the power-frequency droop settings. This functionality will not be influenced by the PLL, which will continue to track the actual frequency of the voltage at the filter capacitors independently of changes in the operating mode.

Non-linear system model

In the following subsections, the mathematical models of the different elements of the system from Fig. 1 are presented as basis for developing a nonlinear mathematical model of the investigated VSM configuration in stand-alone operation. This model captures the main dynamics of the proposed implementation, including the nonlinearity introduced by the active and reactive power

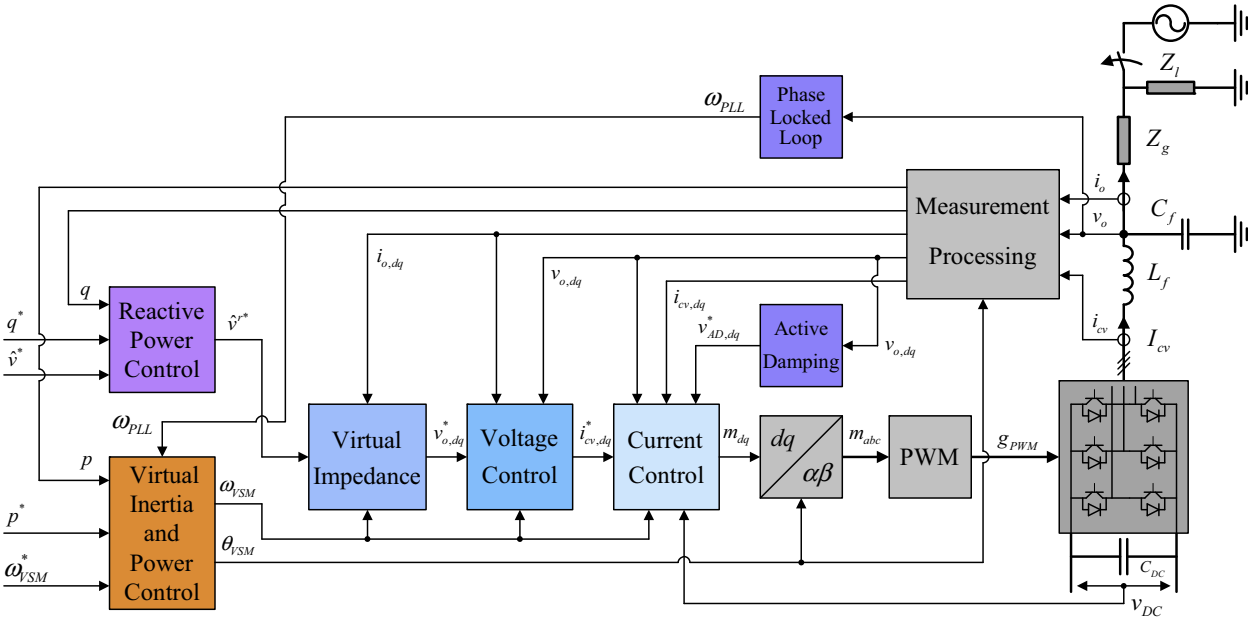

Fig. 1. Overview of investigated system configuration and control structure for the virtual synchronous machine in grid connected and islanded operation.

feedback in the outer loops. However, it should be noted that a modeling based on continuous-time approximations is applied, so the model does not aim to replicate nonlinear effects introduced by the switching operation of the converter or the discrete time implementation of the control system. It is also assumed that the VSM is kept within its normal operating range, so any nonlinear effects caused by saturation of reference signals or by voltage saturation due to limited available dc-voltage are not considered. The resulting nonlinear model will serve as a basis for the derivation of a linearized small-signal model of the VSM in islanded operation while feeding a local load.

Modeling conventions

Upper case symbols in Fig. 1 represent physical values, while the modeling will be presented in per unit quantities, denoted by lower case letters. The base values for the per unit system are defined from the total kVA rating of the converter and the peak value of the rated phase voltage. Transformations of three phase variables into Synchronous Reference Frames (SRFs) are based on the amplitude-invariant Park transformation [26]. Thus, per unit active and reactive powers are defined according to (1). The current directions indicated in Fig. 1 results in positive values for active and reactive powers when flowing towards the grid:

$$\begin{aligned} p &= v_{o,d}\cdot i_{o,d} + v_{o,q}\cdot i_{o,q} \\ q &= -v_{o,d}\cdot i_{o,q} + v_{o,q}\cdot i_{o,d} \end{aligned} \tag{1}$$

Whenever possible, SRF equations will be presented in complex space vector notation according to:

$$\mathbf{x} = x_d + j\cdot x_q \tag{2}$$

Electrical system equations

For modeling of the electrical system, an instantaneous average value model will be used for the VSC. In islanded operation of the VSM, the electrical circuit model from Fig. 1 includes an LC-filter in addition to the series RL equivalents for representing the grid impedance and the load. The state space equations of the AC system in a synchronously rotating reference frame defined by the VSM can then be expressed as given by (3) [12,27].

$$\begin{aligned} \frac{d\mathbf{i}_{cv}}{dt} &= \frac{\omega_b}{l_f}\mathbf{v}_{cv} - \frac{\omega_b}{l_f}\mathbf{v}_o - \left(\frac{r_{lf}\omega_b}{l_f} + j\cdot\omega_{VSM}\omega_b\right)\mathbf{i}_{cv} \\ \frac{d\mathbf{v}_o}{dt} &= \frac{\omega_b}{c_f}\mathbf{i}_{cv} - \frac{\omega_b}{c_f}\mathbf{i}_g - j\cdot\omega_{VSM}\omega_b\cdot\mathbf{v}_o \\ \frac{d\mathbf{i}_o}{dt} &= \frac{\omega_b}{l_g+l_l}\mathbf{v}_o - \left(\omega_b\frac{r_g+r_l}{l_g+l_l} + j\cdot\omega_{VSM}\omega_b\right)\mathbf{i}_o \end{aligned} \tag{3}$$

In these equations $\mathbf{i}_{cv}$ is the current in the converter and filter inductor, $\mathbf{v}_{cv}$ is the converter output voltage, $\mathbf{v}_o$ is the voltage at the filter capacitors and $\mathbf{i}_g$ is the current flowing into the grid or load equivalent. The inductance and equivalent resistance of the filter inductor are given by l_f and r_{lf}, the filter capacitor is c_f, while the inductance and resistance of the grid and the load are given by l_g, r_g, l_l and r_l respectively. The per unit frequency determined by the VSM is given by ω_{VSM}, while the base angular grid frequency is defined by ω_b.

Current controllers and active damping

The inner loop current controllers of the VSM control structure are conventional SRF PI controllers with decoupling terms according to [12,27], and are shown in the right side part of Fig. 2. The output voltage reference from the PI controller is therefore defined by (4), where the resulting voltage reference for the converter is denoted by $\mathbf{v}^*_{cv}$ while the current reference tracked by the controller is given by $\mathbf{i}^*_{cv}$. The proportional and integral gains of the PI controller are defined by k_{pc} and k_{ic}, and $\boldsymbol{\gamma}$ is defined to represent the states for the integrators of the PI controllers according to (5).

$$\mathbf{v}^*_{cv} = k_{pc}(\mathbf{i}^*_{cv} - \mathbf{i}_{cv}) + k_{ic}\cdot\boldsymbol{\gamma} + j\cdot l_f\cdot\omega_{VSM}\cdot\mathbf{i}_{cv} + k_{ffv}\cdot\mathbf{v}_o - k_{AD}(\boldsymbol{\varphi} + \mathbf{v}_o) \tag{4}$$

$$\frac{d\boldsymbol{\gamma}}{dt} = \mathbf{i}^*_{cv} - \mathbf{i}_{cv} \tag{5}$$

In (4), a gain factor k_{ffv}, which can be set to 0 or 1, is used to disable or enable the voltage feed-forward in the output of the controllers. It should be noted that the decoupling terms of the current controllers are based on the per unit angular frequency ω_{VSM} originating from the VSM inertia emulation.

The voltage reference for the converter also includes an active damping term designed for suppressing LC oscillations in the filter [21,22]. The implementation of the active damping algorithm applied in this case is shown in Fig. 3, and the damping voltage reference $\mathbf{v}^*_{AD}$ is based on the difference between the measured filter voltage $\mathbf{v}_o$ and the low pass filtered value of the same voltage, scaled by the gain k_{AD}. The corresponding internal states $\boldsymbol{\varphi}$ are defined by (6), where ω_{AD} is the cut-off frequency of the applied low-pass filters.

$$\frac{d\boldsymbol{\varphi}}{dt} = \omega_{AD}\cdot\mathbf{v}_o - \omega_{AD}\cdot\boldsymbol{\varphi} \tag{6}$$

For the actual implementation of the VSC control system, the voltage reference $\mathbf{v}^*_{cv}$ resulting from the current controller and the active damping is divided by the measured dc-link voltage to

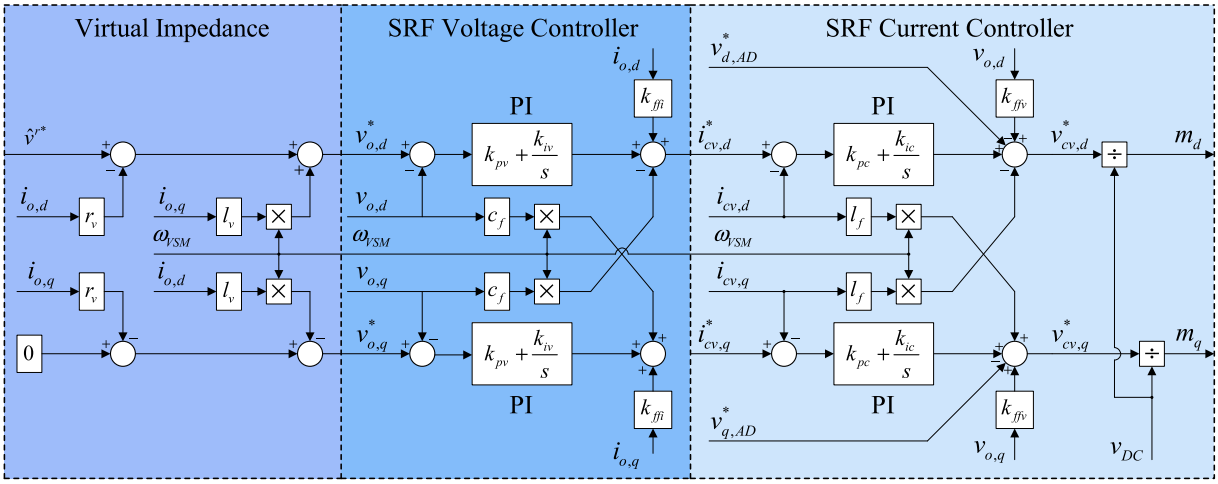

Fig. 2. Virtual impedance, voltage control and current control.

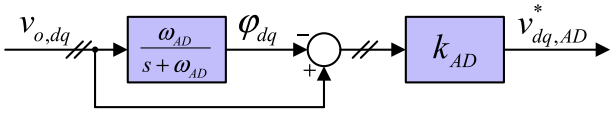

Fig. 3. Active damping.

result in the modulation index **m** as shown to the right of Fig. 2 [23]. Neglecting the delay effect of the PWM implementation, the instantaneous average value of the converter output voltage is given by the product of the modulation index and the actual dc-voltage. Thus, calculating the modulation index by the division indicated in the figure ensures that the per unit output converter voltage will be approximately equal to the voltage reference from the current controller, as summarized by (7). Since this will effectively decouple the AC side control of the converter from variations in the dc voltage, the dynamic response of the dc source does not have to be included in the modeling of the VSM for the purpose of the presented study.

$$\mathbf{m} = \frac{\mathbf{v}^*_{cv}}{v_{DC}}, \qquad \mathbf{v}_{cv} \approx \mathbf{m} \cdot v_{DC} \rightarrow \mathbf{v}_{cv} \approx \frac{\mathbf{v}^*_{cv}}{v_{DC}} \cdot v_{DC} = \mathbf{v}^*_{cv} \tag{7}$$

Voltage controllers and virtual impedance

The structure of the SRF voltage controller for the filter capacitor voltage is shown in the middle of Fig. 2 and is based on the same principles as the current controller [12]. Thus, the current reference used in (4) results from the voltage controller as given by (8). In this equation, the PI controller gains are defined by k_{pv} and k_{iv}, while the gain k_{ffi} is used to enable or disable the feed-forward of measured currents flowing into the grid. The integrator state ξ of the PI controllers is defined by (9).

$$\mathbf{i}^*_{cv} = k_{pv}(\mathbf{v}^*_o - \mathbf{v}_o) + k_{iv}\xi + j \cdot c_f \cdot \omega_{VSM} \cdot \mathbf{v}_o + k_{ffi} \cdot \mathbf{i}_o \tag{8}$$

$$\frac{d\xi}{dt} = \mathbf{v}^*_o - \mathbf{v}_o \tag{9}$$

The voltage reference vector $\mathbf{v}^*_o$ used in (8) and (9) is a result of the voltage amplitude reference $\hat{v}^{r*}$ provided by the reactive power control loop and the virtual impedance. The influence from the virtual resistance r_v and inductance l_v on the capacitor voltage reference is defined on basis of the current $\boldsymbol{i}_o$ according to (10), as illustrated to the left of Fig. 2.

$$\mathbf{v}^*_o = \hat{v}^{r*} - (r_v + j \cdot \omega_{VSM} \cdot l_v) \cdot \mathbf{i}_o \tag{10}$$

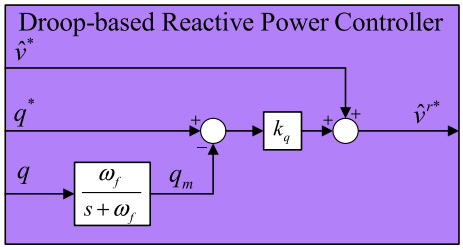

Fig. 4. Reactive power droop controller.

Reactive power droop controller

The droop-based reactive power controller is shown in Fig. 4 and is similar to the controllers commonly applied in microgrid systems as discussed in [12,13]. As shown in the figure, the voltage reference $\hat{v}^{r*}$ used as input to the virtual impedance from (10) is calculated by (11) where $\hat{v}^*$ is the external voltage amplitude reference and q^* is the reactive power reference. The gain k_q is the reactive power droop gain acting on the difference between the reactive power reference and the filtered reactive power measurement q_m. The state of the corresponding low pass filter is defined by (12), where ω_f is the cut-off frequency.

$$\hat{v}^{r*} = \hat{v}^* + k_q(q^* - q_m) \tag{11}$$

$$\frac{dq_m}{dt} = -\omega_f \cdot q_m + \omega_f \cdot q \tag{12}$$

VSM swing equation and inertia emulation

The main difference between a VSM-based control structure and conventional VSC control systems is the inertia emulation by the VSM swing equation. For the investigated VSM implementation, the swing equation is linearized with respect to the speed so that the power balance determines the acceleration of the inertia as shown to the right in Fig. 5 [4,11]. In this figure, p^{r*} is the virtual mechanical input power, p is the measured electrical power, and the mechanical time constant is defined as T_a (corresponding to 2H in a traditional SM). The per unit mechanical speed ω_{VSM} of the virtual inertia is resulting from the integral of the power balance, and the corresponding instantaneous phase angle θ_{VSM} representing the position of the VSM-oriented SRF in the stationary reference frame is given by the integral of the speed. As shown in the figure, the VSM damping power p_d represents the damping effect in a traditional synchronous machine. This damping power is defined by the damping constant k_d and the difference between the VSM speed and the actual grid frequency, which in this case will be provided by a PLL as will be discussed in the following subsection.

For the investigated VSM configuration, an external steady-state frequency droop is also included in the power control of the VSM as shown in the left part of Fig. 5. This frequency control loop is characterized by the droop constant k_ω which is acting on the difference between the frequency reference ω^*_{VSM} and the actual VSM speed. The system also has an external power reference input or set-point given by p^*. Thus, the total power balance of the VSM inertia can be expressed by:

$$\frac{d\omega_{VSM}}{dt} = \frac{p^*}{T_a} - \frac{p}{T_a} - \frac{k_d(\omega_{VSM} - \omega_{PLL})}{T_a} + \frac{k_\omega(\omega^*_{VSM} - \omega_{VSM})}{T_a} \tag{13}$$

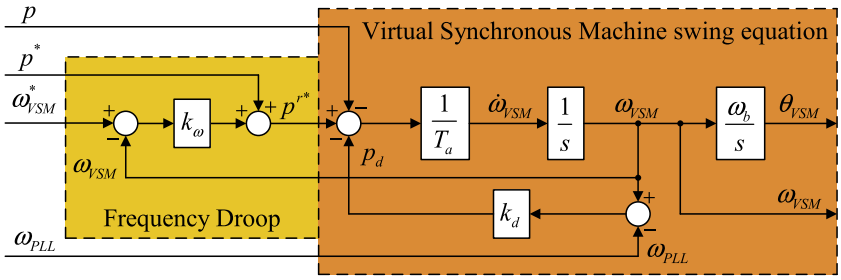

Fig. 5. Virtual synchronous machine inertia emulation with power-frequency droop.

During islanded operation, the system frequency is determined by the VSM speed, and there is no phase displacement between the VSM internal voltage and any external voltage source that must be explicitly modeled. Thus, the phase orientation of the SRF does not have to be represented for a model defined in the VSM-oriented SRF, and the state-space model for the VSM in islanded operation will have one state less than the model for grid connected operation from [14]. The instantaneous phase angle θ_{VSM} associated with the VSM inertia will, however, be defined directly according to the block diagram of Fig. 5, as given by (14). As for the model in grid connected mode, this will be a saw-tooth signal between 0 and 2π which will be used for transformations between the SRF defined by the VSM inertia and the three phase electrical system as indicated in Fig. 1, but it will not be represented as a state variable in the VSM-oriented SRF model.

$$\frac{d\theta_{VSM}}{dt} = \omega_{VSM} \cdot \omega_b \tag{14}$$

Phase locked loop

The basic scheme of the Phase Locked Loop (PLL) used to track the frequency of the voltage at the filter capacitors is based on [17,18] and its structure is shown in Fig. 6. This PLL is using first order low-pass filters on the estimated d- and q-axis voltages and an inverse tangent function to estimate the actual phase angle error of the PLL. This phase angle error is the input to a PI controller which is used to eliminate the frequency error with respect to the speed of the VSM. Thus, the VSM speed is used as a feed-forward signal in the PLL, as indicated in the figure. This is a similar approach as used in the recently proposed PLLs with secondary control path [24,25], where a dynamic feed-forward of estimated frequency is used as an offset to the output of the PI-controller of the PLL. However, the frequency feed-forward is in this case not an estimate, since the actual VSM frequency is directly available in the control system. The resulting frequency ω_{PLL} estimated by the PLL is integrated to obtain the estimate of the corresponding phase angle.

The states of the low-pass filters of the PLL, resulting in the filtered voltage $\mathbf{v}_{PLL}$, is given by (15), where the last term shows the transformation of the voltage vector $\mathbf{v}_o$ into the local reference frame defined by the PLL. The cut-off frequency of the applied low pass filters is given by $\omega_{LP,PLL}$.

$$\frac{d\mathbf{v}_{PLL}}{dt} = -\omega_{LP,PLL} \cdot \mathbf{v}_{PLL} + \omega_{LP,PLL} \cdot \mathbf{v}_o e^{-j\delta\theta_{PLL}} \tag{15}$$

The integrator state ε_{PLL} of the PI controller is defined by (16), and the per unit speed deviation $\delta\omega_{PLL}$ between the SRFs defined by the PLL and the VSM is defined by (17) for SRF-based small-signal modeling. The corresponding phase angle difference $\delta\theta_{PLL}$ between the local reference frame defined by the PLL and the VSM-oriented reference frame, is defined by (18), in a similar way as described for the grid connected operation in [14].

$$\frac{d\varepsilon_{PLL}}{dt} = \arctan\left(\frac{v_{PLL,q}}{v_{PLL,d}}\right) \tag{16}$$

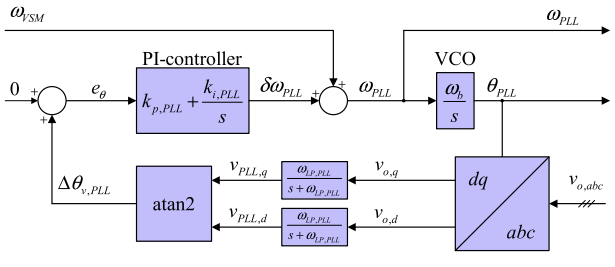

Fig. 6. Phase locked loop.

$$\delta\omega_{PLL} = k_{p,PLL} \cdot \arctan\left(\frac{v_{PLL,q}}{v_{PLL,d}}\right) + k_{i,PLL} \cdot \varepsilon_{PLL} \tag{17}$$

$$\frac{d\delta\theta_{PLL}}{dt} = \delta\omega_{PLL} \cdot \omega_b \tag{18}$$

The actual per unit frequency ω_{PLL} detected by the PLL is defined by (19), and will always settle to the same value as the VSM speed in steady state. In the same way as for the VSM, the phase angle used for the transformation of the measured three phase voltages into the local SRF defined by the PLL is defined by θ_{PLL} according to (20).

$$\omega_{PLL} = \delta\omega_{PLL} + \omega_{VSM} \tag{19}$$

$$\frac{d\theta_{PLL}}{dt} = \omega_{PLL} \cdot \omega_b \tag{20}$$

Reference frame transformations

Considering the control system in Fig. 1, the VSM swing equation in Fig. 5 and the explanations in the previous subsections, it should be clear that the entire control system except for the PLL is implemented in a SRF defined by the angular position θ_{VSM} of the VSM virtual inertia. Thus, the electrical circuit is also modeled in the same VSM-oriented SRF, while the PLL is defining a local SRF based on the voltages at the filter capacitors. For the investigated case of islanded operation, the phase angle orientation of the PLL is defined with respect to the VSM-oriented SRF by $\delta\theta_{PLL}$. This angle can also be considered as the difference between the instantaneous phase angle θ_{VSM} of the VSM internal voltage and the estimated phase angle θ_{PLL} of the filter capacitor voltages. An overview of the voltage vectors and phase angles defining the SRF transformations of the control system is shown in Fig. 7. This figure indicates how the dq reference frame defined by the VSM is used as the main SRF orientation for the modeling of the system. From the phase angles defined in the vector diagram, it is also clearly seen how θ_{VSM} and θ_{PLL} are representing the actual phase angles used for transformations between the stationary reference frame and the SRFs used for controller implementation and modeling of the system. The figure also shows how $\delta\theta_{PLL}$ defined by (18) represents the phase displacement between the VSM-oriented and PLL-oriented SRFs.

Linearized system model

A non-linear state-space model of the electrical grid and the VSM control system can be established by reducing the equations

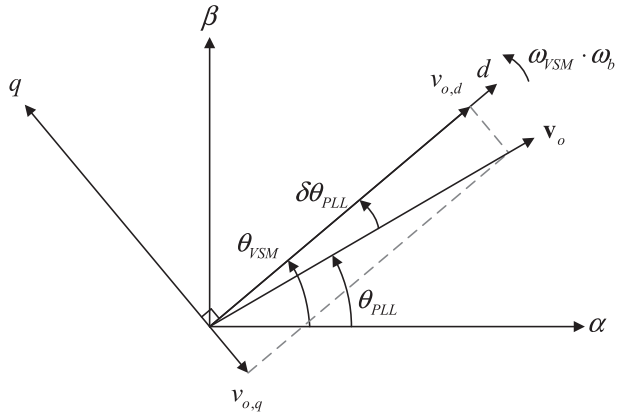

Fig. 7. Vector diagram defining the VSM-oriented SRF and corresponding phase angles.

presented in the previous section, and the resulting set of equations is given by (24) in the Appendix A. The state variables **x** and input signals **u** of the investigated VSM model for islanded operation are listed in (21), resulting in a state space model of 18th order.

$$\mathbf{x} = [\, v_{o,d} \quad v_{o,q} \quad i_{cv,d} \quad i_{cv,q} \quad \gamma_d \quad \gamma_q \quad i_{o,d} \quad i_{o,q} \quad \varphi_d \quad \varphi_q \quad v_{PLL,d} \quad v_{PLL,q} \quad \varepsilon_{PLL} \quad \xi_d \quad \xi_q \quad q_m \quad \omega_{VSM} \quad \delta\theta_{PLL} \,]^T$$
$$\mathbf{u} = [\, p^* \quad q^* \quad \hat{v}^* \quad \omega^* \,]^T \tag{21}$$

The corresponding linearized small-signal state space model of the system can be found from the non-linear model in (24) and defined on the general form given by (22) [26].

$$\Delta\dot{\mathbf{x}} = \mathbf{A} \cdot \Delta\mathbf{x} + \mathbf{B} \cdot \Delta\mathbf{u} \tag{22}$$

The model defined by (22) is only expressing small-signal deviations around the point of linearization, and the states and inputs are therefore denoted by Δ. For the elements in the **A** and **B** matrices depending on the linearization point of the system, the initial operating points of the states are denoted by subscript 0 and must be found by solving for the steady state solution of (24) with a given set of reference signals and system parameters. The elements of the resulting small-signal state-space equation of the VSM are presented by Eqs. (26)–(29) in the Appendix A.

Analysis of The VSM in islanded operation

This section analyses the behavior of the proposed VSM implementation in islanded operation. The presented analysis is intended to complement the studies of the same control system in grid connected operation from [14] and [15]. Thus, together these studies should provide a comprehensive analysis of the functional behavior and dynamic characteristics of the investigated VSM scheme in both grid connected and stand-alone operation. For this reason, the main system parameters used for the simulations and numerical analysis, as listed in Table 1, are maintained the same as in [14]. In addition to the parameters listed in the table, it should be mentioned that the active damping is disabled by setting the gain k_{AD} equal to zero and that the voltage feed-forward for the current controller is enabled while the current feed-forward for the voltage controller is disabled.

As a starting point, the inherent ability of the investigated VSM implementation to operate in both grid connected and stand-alone modes is demonstrated by a simulation example showing the response to a sudden islanding condition. Then, the validity of the linearized model for islanded operation developed in the previous sections is verified by numerical simulations before it is used to analyze the eigenvalues and parametric sensitivities of the VSM when feeding a local load.

Simulated response to sudden islanding

As already explained, an essential feature characterizing the investigated VSM implementation is the possibility to operate both in grid connected and islanded mode. Moreover, the transition between the two operating modes is almost seamless and does not require any modification to the internal control configuration or controller settings, and transition from grid connected to islanded operation does not depend on any islanding detection algorithm. To demonstrate this, an example of a sudden transition from grid connected operation to islanded mode while feeding a local load has been simulated numerically in the Matlab/Simulink environment, based on the system configuration from Fig. 1 and the parameters listed in Table 1. The simulation model includes a full representation of the electrical system by the SimPowerSystems block-set of Simulink, with the only simplification that an ideal average model of the converter, represented as a controllable three-phase voltage source, is used for the VSC.

The main results from the simulation are displayed in Figs. 8 and 9. The VSM is initially in steady state operation, connected to a grid represented by an ideal voltage source. The power reference for the VSM is set to 0.7 pu and the frequency reference as well as the grid frequency are equal to 1.0 pu. As shown in Fig. 8(a), the output power of the VSM is following its reference value when the system is grid connected. Then, at time $t = 0.5$ s, the grid is disconnected and the VSM unit remains connected to a local load represented by a simple RL-equivalent with a resistance of 2.0 pu and an inductance of 0.2 pu. When the islanding condition occurs, the output power from the VSM is rapidly decreased to approximately 0.44 pu which is the sum of the power consumed by the load and the resistive losses of the grid equivalent. The change in the power output is also reflected in the output current from the VSM as pictured in Fig. 8(b). The response in the voltage amplitude at the filter capacitors is shown in Fig. 8(c), and after a short transient due to the breaker operation in the grid, there is a small drop in voltage due to the reactive power consumption of the local load. The response in the speed of the VSM is shown in Fig. 9, and since the local load is lower than the power reference, the frequency is increased in response to the islanding condition. However, the VSM unit manages to preserve the voltage amplitude and frequency within the normal operating range, and the load experiences less than 4% variation in voltage and less than 1.5% variation in the steady-state frequency. It should be emphasized that during the transition, the external references and the

Table 1
Parameters of investigated VSM configuration in islanded operation.

Parameter	Value	Parameter	Value (pu)
Rated voltage, $V_{S,LL,RMS}$	690 V	Filter inductance, l_f	0.08
Rated power, S_b	2.75 MVA	Filter resistance, r_{lf}	0.003
Rated angular frequency, ω_b	$2\pi^*50$ Hz	Filter capacitance, c_f	0.074
VSM Inertia constant, T_a	2 s	Grid inductance, l_g	0.20
VSM Damping coefficient, k_d	400	Grid resistance, r_g	0.01
Current controller gains, k_{pc}, k_{ic}	1.27, 14.3	Load inductance, l_l	0.2
Voltage controler gains, k_{pv}, k_{iv}	0.59, 736	Load resistance, r_l	2.0
Power reference, grid connected, p^*	0.7 pu	Virtual inductance, l_v	0.2
Speed reference, ω^*	1.0 pu	Virtual resistance, r_v	0.0
Voltage reference, $\hat{v}^*$	1.0 pu	Power droop gain, k_ω	20
Reactive power reference, q^*	0.0 pu	Reactive power droop gain, k_q	0.2

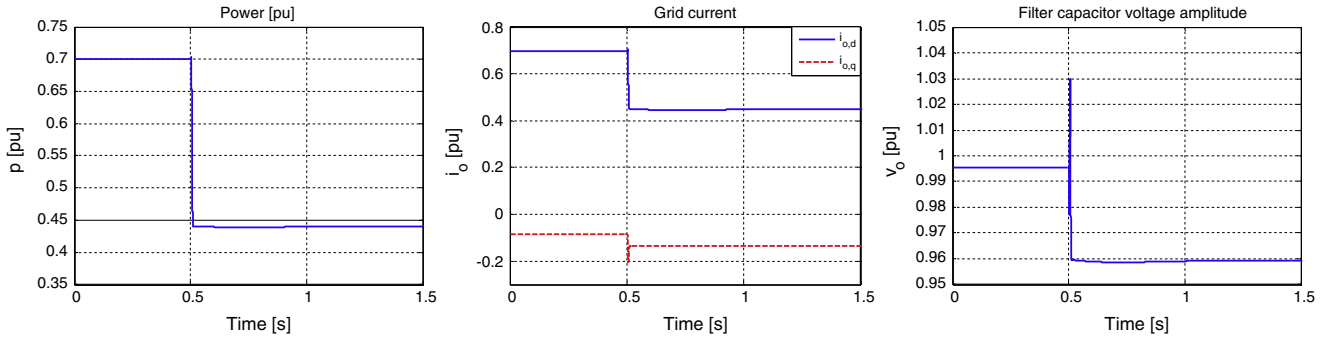

(a) VSM output power (b) Output current d- and q- components (c) Voltage amplitude at filter capacitors

Fig. 8. Power flow, voltage and current from the VSM in response to a sudden islanding condition.

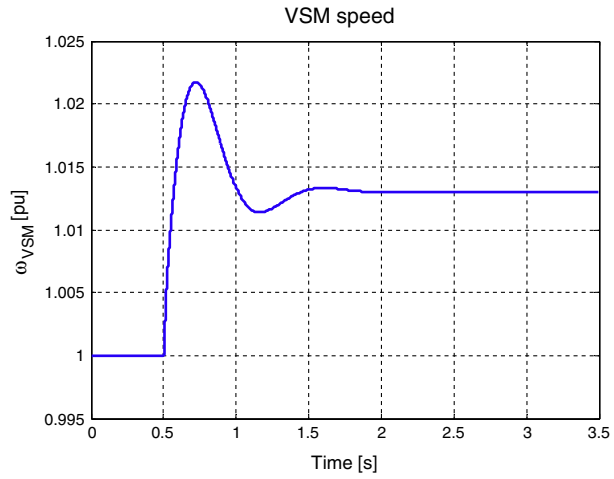

Fig. 9. VSM speed resulting from a sudden islanding condition.

internal controller settings are unaltered, but still another steady state condition is reached smoothly within approximately 1.5 s. The VSM speed exhibits a classical damped oscillatory behavior similar to a synchronous machine, while the power, voltages and currents adapt to the new operating conditions through a much faster, well damped, transient response.

Model validation

The validity of the small-signal state-space model documented in Appendix A is verified by comparing its dynamic response to the response of a non-linear simulation model. The same model as applied for the simulations shown in the previous sub-section is applied with only minor modifications in the signal routing to allow for direct comparison with a parallel simulation of the linearized state-space model.

The model validity has been verified for the full operating range of the VSM by multiple simulations, but will be illustrated for one particular example by the following figures. For this simulation case, a steady-state operating point with an active power reference of 0.44 pu, resulting in VSM speed equal to the reference value of 1.0 pu while feeding the local RL load in islanded mode, is used for the linearization. However, the system is initially simulated with a power reference of 0.7 pu corresponding to the same operating conditions as resulting from the sudden islanding condition simulated in the previous sub-section. At time $t = 0.5$ s, the power reference is stepped down to the value of 0.44 pu as used for the linearization.

Comparisons of the response obtained with the electrical simulation model and the linearized small-signal state-space model are shown in Figs. 10–12. The results in Fig. 10(a) clearly show that the speed response of the VSM, and thus the power-balance-dependent operating frequency of the system, is accurately represented by the small-signal model. Similarly, the voltage amplitude at the filter capacitors and the output power of the VSM, which can be calculated from the state variables of the small-signal model, are also coinciding with the results from the nonlinear electrical simulation model. The phase angle displacement between the VSM orientation and the local SRF defined by the PLL is shown in Fig. 11, and is also accurately represented by the small signal model. The d- and q-axis components of the output currents from the VSM are shown in Fig. 12, and in this case a very small deviation can be seen between the two models. Although it might be expected that the operation before time

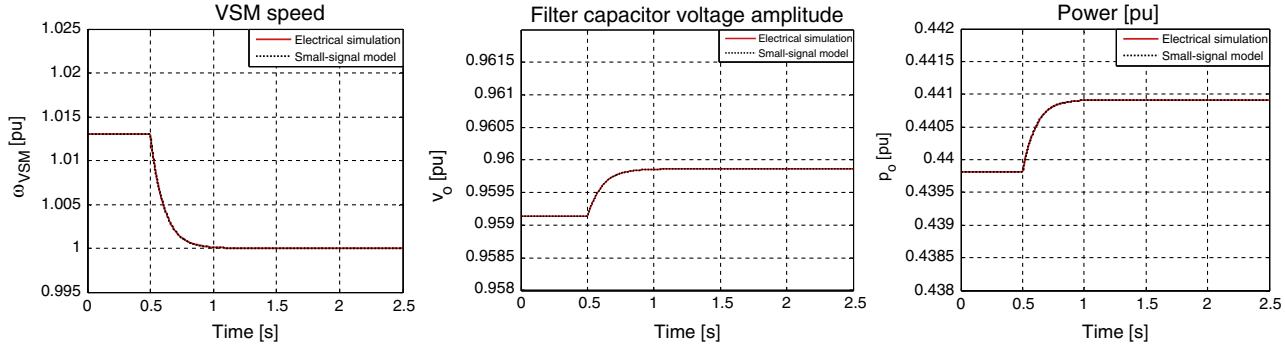

(a) Response in VSM speed (b) Response in voltage amplitude (c) Response in power flow

Fig. 10. Comparison of step response in active power output, filter capacitor voltage and VSM speed resulting from nonlinear simulations and the linearized small-signal model when the active power reference is stepped down from 0.7 pu to the actual load of the system.

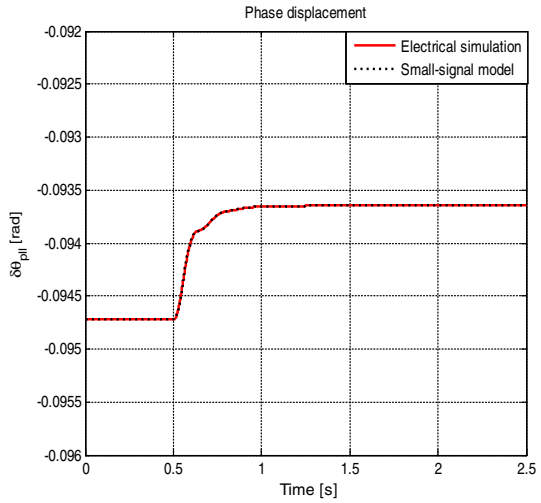

Fig. 11. Comparison of phase angle displacement between the PLL- and VSM-oriented reference frames resulting from the nonlinear simulation and the linearized small-signal model.

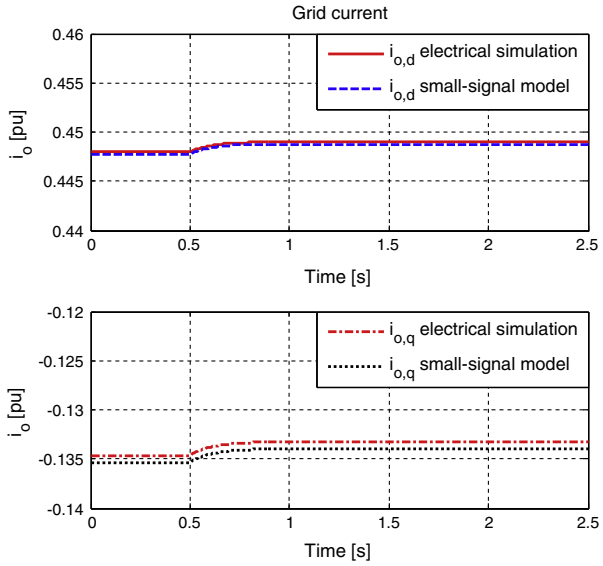

Fig. 12. Comparison of grid side current components resulting from nonlinear simulations and the linearized small-signal model.

t = 0.5 s should show some deviations since the small-signal model is then operating away from the linearization point, a small deviation can also be observed in the steady-state operation corresponding to the linearization point. This is mainly because the detailed electrical simulation model inherently implies minor delays associated with the numerical implementation and the transformations between the different reference frames, while these effects are not represented in the small-signal state-space model. However, the deviations are very small, and most of the curves produced by the two models are practically overlapping. Thus, the presented results clearly demonstrate that the linearized model can accurately capture the dynamic response of the system. It should be noted that a similar degree of accuracy is obtained also for the other state variables in the system, and that the accuracy is not much affected by the operating conditions and the corresponding linearization point.

From the plotted results, it can be observed that the step change in the power reference leads to an over-damped transient response and that the system reaches a new steady-state condition in approximately 0.5 s. As expected, the frequency is slightly reduced when the power reference is reduced, as shown in Fig. 10(a). The voltage amplitude and the output active power are slightly increased, and the main reason for this is that the reduced frequency leads to a reduced voltage drop across the internal virtual impedance of the VSM, which again causes higher output voltage and accordingly higher power consumption in the load resistance. From the plotted curves it should also be noticed that the system shows a more damped response than usually expected from a traditional SM. This is because the damping of the VSM can be specified to a high value without considering any of the design constraints influencing the parameters of a physical SM.

System eigenvalue analysis

Since the developed linearized small-signal model has been shown to accurately represent the investigated system, the eigenvalues of the **A** matrix can be calculated to systematically identify all the modes of the system. All the system eigenvalues for the steady-state operating point corresponding to islanded operation with 0.44 pu power reference are listed in Table 2. For studying system stability, the slow and poorly damped poles will be of main interest, and from the listed poles it can be noticed that the system has several real poles and one pair of complex conjugate poles close to the origin. There are also two pairs of poles with a relatively high oscillation frequency associated with the LC resonances in the system. However, in the case of islanded operation with a local RL-load, the damping of these poles is significantly higher than for the case of grid connected operation discussed in [14]. This is mainly because the resistance of the local RL-load is directly introducing more damping to the electrical circuit compared to the case of grid connected operation.

As already seen from the time-domain simulations, the system is stable with the parameters and operating conditions specified in Table 1. However, the small-signal model can easily be utilized to further investigate the dynamic characteristics of the system under various operating conditions and with various system parameters. As a first example, the eigenvalue trajectory of the system when sweeping the active power reference in the full operating range from −1.0 pu to 1.0 pu is shown in Fig. 13(a) where the color gradient from blue towards red indicate the change of the power reference. As already explained, the steady state frequency and operating conditions of the system will change if the power reference is changed while the load is kept constant. However, the pole trajectory in Fig. 13(a) shows that the system eigenvalues are not much influenced by the change of power reference, indicating that variations in the steady-state operating frequency due to the power-frequency droop will not have significant impact on the dynamic response of the VSM.

A further investigation on how changes of system parameters are influencing the dynamic response of the investigated VSM configuration is shown in Fig. 13(b) and (c) where the load resistance is swept from a high load case of 0.9 pu to 1000 pu corresponding to almost open circuit, no-load, conditions. An overview of the

Table 2
System eigenvalues under stand-alone operation.

$\lambda_1 = -20$	$\lambda_{11,12} = -639 \pm j\ 169$
$\lambda_2 = -20$	$\lambda_{13} = -4722$
$\lambda_3 = -500$	$\lambda_{14,15} = -13 \pm j\ 38$
$\lambda_{4,5} = -1351 \pm j\ 3\ 226$	$\lambda_{16} = -9.5$
$\lambda_{6,7} = -1124 \pm j\ 3\ 058$	$\lambda_{17} = -11.2$
$\lambda_{8,9} = -3465 \pm j\ 297$	$\lambda_{18} = -11.2$
$\lambda_{10} = -1001$	

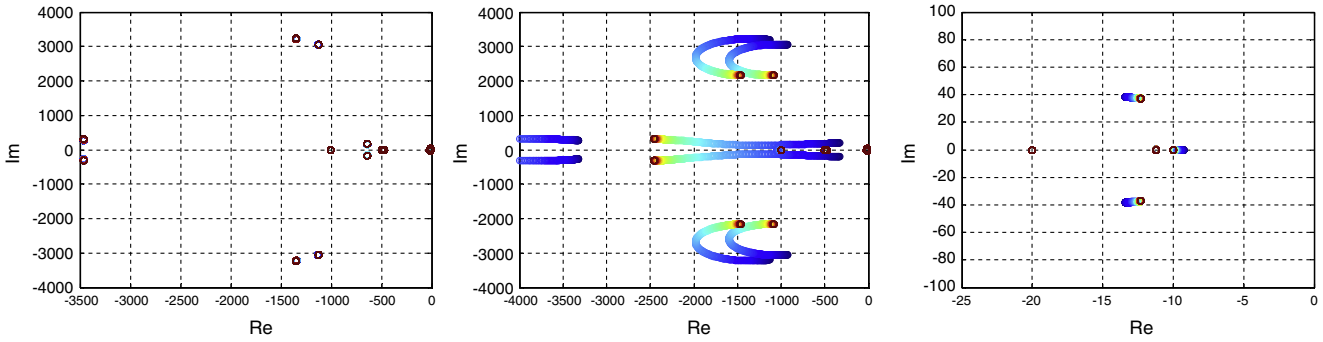

(a) System eigenvalue trajectory with power reference p^* swept from −1.0 pu to 1.0 pu

(b) System eigenvalue trajectory with load resistance r_l swept from 0.9 pu to 1000 pu

(c) Zoom of system eigenvalue trajectory with load resistance r_l swept from 0.9 pu to 1000 pu

Fig. 13. Impact of power reference and load resistance on system eigenvalues.

resulting trajectories for all the system eigenvalues is shown in Fig. 13(b) while a zoom of the eigenvalues closest to the origin is shown in Fig. 13(c). From these figures, it is clearly seen that the oscillatory eigenvalues associated with the LC resonances in the system are strongly influenced by the load resistance, which is directly influencing the damping of the electrical system. When the load resistance is increasing, these eigenvalues start moving towards the right but if the load resistance becomes very large, i.e. when the load becomes very low, they start moving towards the right again while almost no current will flow towards the load. It can also be seen that two sets of complex conjugate pole pairs with low oscillation frequency are monotonously moving towards the right when the load resistance increases, and this is because these modes are related to the RL-time constants of the system. Thus, most oscillatory modes in the system will always be more damped for the islanded operation with a local RL-load than for the grid connected operation analyzed in [14]. However, if the load is not passive, but instead represented by a controlled converter, the eigenvalues associated with LC-oscillations in the electrical system will have a stronger influence on the system dynamics in a similar way as for the operation in grid connected mode [14].

Observing the zoom of the trajectories for the slowest eigenvalues of the system shown in Fig. 13(c), it can be noticed that they are not much influenced by the load resistance. Thus, the dominant transient responses to small variations in system operating conditions will not strongly depend on the loading of the system. However, further analysis of the system eigenvalues can be applied to reveal and understand how the different eigenvalues are influenced by the system parameters and how the system can be tuned to improve the dynamic response.

Parameter sensitivity of dominant system eigenvalues

Investigation of the system stability by ad hoc variations of the controller parameters and corresponding calculation of system poles is challenging for a high order system as the investigated VSM. Instead, the sensitivity of the most critical poles with respect to the system parameters can be investigated in order to reveal which parameters will influence the different eigenvalues and for identifying measures that might ensure system stability and satisfactory dynamic response.

The parameter sensitivity of the system poles is defined as the derivative of the eigenvalues with respect to the system parameters. For a dynamic system of order N and with a set of K tunable parameters, the sensitivities define a sensitivity matrix of N by K complex elements. The relative sensitivity $\alpha_{n,k}$ of the eigenvalue λ_n with respect to the parameter ρ_k can be expressed by (23), where $\mathbf{\Psi}_n^T$ and $\mathbf{\Phi}_n$ are the left and right eigenvectors associated to the eigenvalue λ_n [26,28].

$$\alpha_{n,k} = \frac{\partial \lambda_n}{\partial \rho_k} = \frac{\mathbf{\Phi}_n^T \frac{\partial \mathbf{A}}{\partial \rho_k} \mathbf{\Psi}_n}{\mathbf{\Phi}_n^T \mathbf{\Psi}_n} \tag{23}$$

The real part of the sensitivities is directly associated to the derivatives of the pole location along the real axis with respect to each parameters, where a positive value means that an increase of the actual parameter will move the corresponding pole to the right. Similarly, the imaginary part of the sensitivity is associated to the derivative of the pole location along the imaginary axis. However, since the real parts of the pole locations determine the stability and the corresponding time constant of the associated system mode, only the real part of the sensitivity matrix will be investigated in the following.

Examples of the calculated parametric sensitivities for two of the system poles are plotted in Figs. 14 and 15, where Fig. 14 shows the parameter sensitivity of the slowest pole in the system, while Fig. 15 shows the parameter sensitivity of the slowest complex conjugate pole pair in the system. From Fig. 14, it can be noticed that the slowest pole is mainly dependent on the mechanical time constant, the frequency droop gain and the virtual impedance, and could be made faster by reducing T_a or l_v, or by increasing k_ω or r_v. However, since this pole is not much influenced by any of the other parameters, it is also unlikely to cause instability in the system. Thus, this pole might be dominant in the transient response for any of the system states, but is not a critical pole in the sense that it can easily cause instability.

The complex conjugate pole pair studied in Fig. 15 is also significantly influenced by the virtual impedance and the mechanical time constant, but is further influenced by the integral gain of the PLL and the total equivalent resistance r_t and inductance l_t resulting from the series connection of the grid equivalent and the RL-load. Since all of these parameters, except for the system impedance, can be selected during the control system design and will not change due to external conditions during normal operation, it is also unlikely that this pole pair will cause instability. However, it should be noted that although the controller parameters can be utilized to speed-up the transient response of this mode, the mechanical time constant and the virtual impedance will usually be selected according to other criteria. Thus, it is limited how much the transient response of this pole pair can be improved without degrading the intended performance of the VSM. On the other hand, it is again demonstrated how the investigated VSM implementation has a faster and more damped response when feeding a local load under islanding conditions than

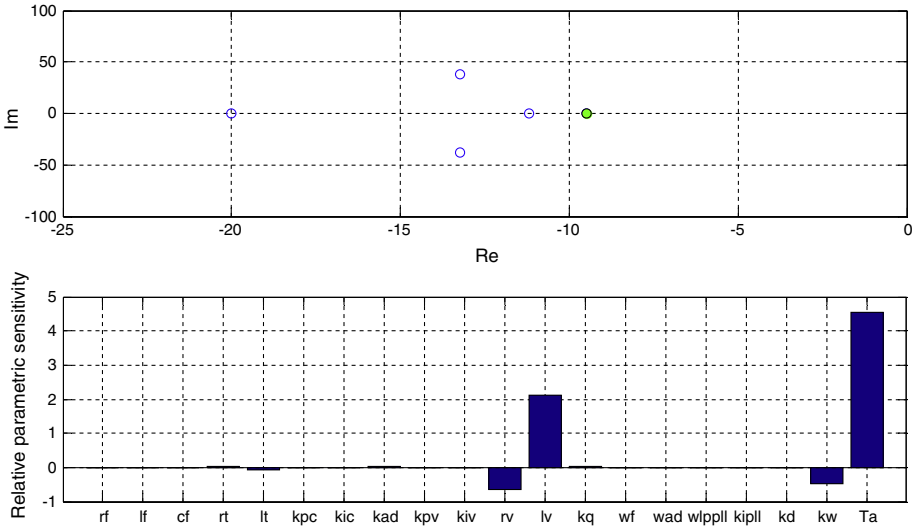

Fig. 14. Parametric sensitivity of the pole with the highest real value.

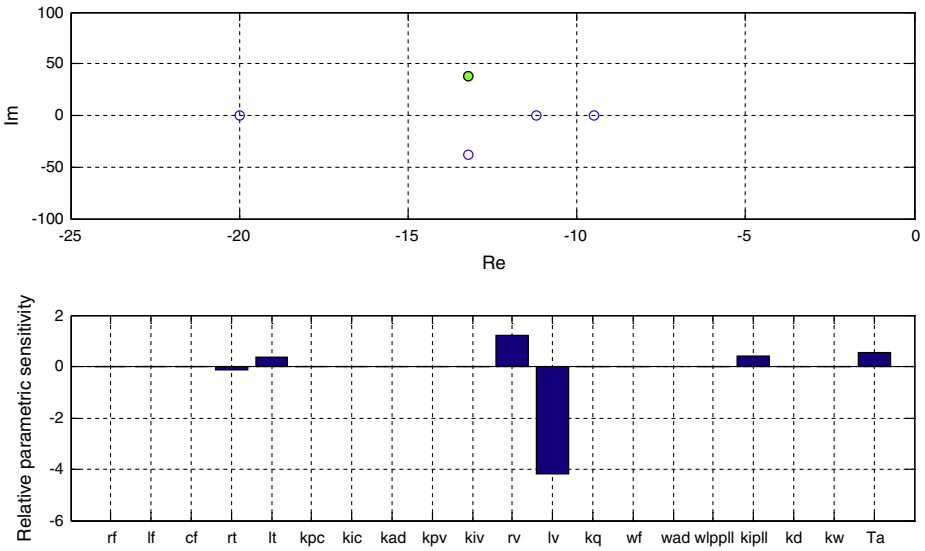

Fig. 15. Parametric sensitivity of the complex conjugate pole pair with the highest real part.

when connected to the grid. In case it is possible to identify operating conditions or special events where the system eigenvalues are close to the stability limit or the system has poor dynamic performance due to poles located close to 0, the parameter sensitivities can be used for the tuning of the system, either by manual analysis or by automated iterative procedures as investigated in [11,29].

Conclusion

This paper has presented the detailed modeling and analysis of a Virtual Synchronous Machine (VSM) configuration operated under islanded conditions. The VSM inertia emulation is based on the simplified swing equation of traditional synchronous machines and provides a power-balance-based grid synchronization of the converter control system when connected to an external grid. However, the same swing equation can also establish the power balance and corresponding operating frequency under islanded operation. This has been demonstrated by simulations, showing a seamless transfer from grid connected to stand-alone operation of the VSM. Each individual element of the investigated control system has also been presented in detail, and the corresponding equations needed for developing a linearized small-signal model of the overall system under islanded conditions have been derived. The validity of the developed small-signal model has been verified by comparison to a simulation model of the system including the nonlinearities, and has been applied to analyze the system eigenvalues and their sensitivities with respect to the system parameters. Combined with the results from previous investigations of the VSM under grid connected operation, the presented results for islanded operation are providing enhanced insight into the dynamic characteristics and internal modes of the investigated VSM configuration under various operating conditions.

Acknowledgement

The work of SINTEF Energy Research in this paper was supported by the project "Releasing the Potential of Virtual Synchronous Machines – ReViSM" through the Blue Sky instrument of SINTEF Energy Research as a Strategic Institute Programme (SIP) financed by the national Basic Funding Scheme of Norway

Appendix A. State-space model

A.1. Non-linear state-space model

The non-linear state-space model of the investigated VSM configuration in islanded operation can be found by reducing the equations presented in the section 'Non-linear system model' to state-space form, and is defined by:

$$\frac{dv_{o,d}}{dt} = \omega_b\omega_{VSM}v_{o,q} + \frac{\omega_b}{c_f}i_{cv,d} - \frac{\omega_b}{c_f}i_{o,d}$$

$$\frac{dv_{o,q}}{dt} = -\omega_b\omega_{VSM}v_{o,d} + \frac{\omega_b}{c_f}i_{cv,q} - \frac{\omega_b}{c_f}i_{o,q}$$

$$\frac{di_{cv,d}}{dt} = \frac{\omega_b\left(k_{ffv}-1-k_{AD}-k_{pc}k_{pv}\right)}{l_f}v_{o,d} - \frac{\omega_b c_f k_{pc}}{l_f}\omega_{VSM}v_{o,q} - \frac{\omega_b\left(k_{pc}+r_f\right)}{l_f}i_{cv,d} + \frac{\omega_b k_{ic}}{l_f}\gamma_d + \frac{\omega_b k_{pc}\left(k_{ffi}-k_{pv}r_v\right)}{l_f}i_{o,d} + \frac{\omega_b k_{pc}k_{pv}l_v}{l_f}\omega_{\omega_{VSM}}i_{o,q} + \frac{\omega_b k_{AD}}{l_f}\varphi_d + \frac{\omega_b k_{iv}k_{pc}}{l_f}\xi_d - \frac{\omega_b k_{pc}k_{pv}k_q}{l_f}q_m + \frac{\omega_b k_{pc}k_{pv}k_q}{l_f}q^* + \frac{\omega_b k_{pc}k_{pv}}{l_f}\hat{v}^*$$

$$\frac{di_{cv,q}}{dt} = \frac{\omega_b c_f k_{pc}}{l_f}\omega_{VSM}v_{o,d} + \frac{\omega_b\left(k_{ffv}-1-k_{AD}-k_{pc}k_{pv}\right)}{l_f}v_{o,q} - \frac{\omega_b\left(k_{pc}+r_f\right)}{l_f}i_{cv,q} + \frac{\omega_b k_{ic}}{l_f}\gamma_q - \frac{\omega_b k_{pc}k_{pv}l_v}{l_f}\omega_{VSM}i_{o,d} + \frac{\omega_b k_{pc}\left(k_{ffi}-k_{pv}r_v\right)}{l_f}i_{o,q} + \frac{\omega_b k_{AD}}{l_f}\varphi_q + \frac{\omega_b k_{iv}k_{pc}}{l_f}\xi_q$$

$$\frac{d\gamma_d}{dt} = -k_{pv}v_{o,d} - c_f\omega_{VSM}v_{o,q} - i_{cv,d} + \left(k_{ffi}-k_{pv}r_v\right)i_{o,d} + k_{pv}l_v\omega_{VSM}i_{o,q} + k_{iv}\xi_d - k_{pv}k_q q_m + k_{pv}k_q q^* + k_{pv}\hat{v}^*$$

$$\frac{d\gamma_d}{dt} = c_f\omega_{VSM}v_{o,d} - k_{pv}v_{o,q} - i_{cv,q} - k_{pv}l_v\omega_{VSM}i_{o,d} + \left(k_{ffi}-k_{pv}r_v\right)i_{o,q} + k_{iv}\xi_q$$

$$\frac{di_{o,d}}{dt} = \frac{\omega_b}{l_g}v_{o,d} - \frac{\omega_b r_g}{l_g}i_{o,d} + \omega_b\omega_{VSM}i_{o,q}$$

$$\frac{di_{o,q}}{dt} = \frac{\omega_b}{l_g}v_{o,q} - \omega_b\omega_{VSM}i_{o,d} - \frac{\omega_b r_g}{l_g}i_{o,q}$$

$$\frac{d\varphi_d}{dt} = \omega_{AD}v_{o,d} - \omega_{AD}\varphi_d$$

$$\frac{d\varphi_q}{dt} = \omega_{AD}v_{o,q} - \omega_{AD}\varphi_q$$

$$\frac{dv_{PLL,d}}{dt} = \omega_{LP,PLL}v_{o,d}\cos\left(\delta\theta_{PLL}\right) + \omega_{LP,PLL}v_{o,q}\sin\left(\delta\theta_{PLL}\right) - \omega_{LP,PLL}v_{PLL,d}$$

$$\frac{dv_{PLL,q}}{dt} = -\omega_{LP,PLL}v_{o,d}\sin\left(\delta\theta_{PLL}\right) + \omega_{LP,PLL}v_{o,q}\cos\left(\delta\theta_{PLL}\right) - \omega_{LP,PLL}v_{PLL,q}$$

$$\frac{d\varepsilon_{PLL}}{dt} = \tan^{-1}\left(\frac{v_{PLL,q}}{v_{PLL,d}}\right)$$

$$\frac{d\delta\xi_d}{dt} = -v_{o,d} - r_v i_{o,d} + l_v\omega_g i_{o,q} - k_q q_m + l_v i_{o,q}\omega_{VSM} + k_q q^* + \hat{v}^*$$

$$\frac{d\delta\xi_q}{dt} = -v_{o,q} - l_v\omega_g i_{o,d} - r_v i_{o,q} - l_v i_{o,d}\omega_{VSM}$$

$$\frac{dq_m}{dt} = -\omega_f i_{o,q}v_{o,d} + \omega_f i_{o,d}v_{o,q} - \omega_f q_m$$

$$\frac{d\delta\theta_{VSM}}{dt} = -\frac{1}{T_a}i_{o,d}v_{o,d} - \frac{1}{T_a}i_{o,q}v_{o,q} + \frac{k_d k_{p,PLL}}{T_a}\tan^{-1}\left(\frac{v_{PLL,q}}{v_{PLL,d}}\right) + \frac{k_d k_{i,PLL}}{T_a}\varepsilon_{PLL} + \frac{1}{T_a}p^* + \frac{k_\omega}{T_a}\omega^*_{VSM} - \frac{k_\omega}{T_a}\omega_{VSM}$$

$$\frac{d\delta\theta_{PLL}}{dt} = \omega_b k_{p,PLL}\tan^{-1}\left(\frac{v_{PLL,q}}{v_{PLL,d}}\right) + \omega_b k_{i,PLL}\varepsilon_{PLL} \tag{24}$$

A.2. Linearized small-signal state-space model

The states and the **A**-matrix of the investigated VSM configuration are in the following written according to (25), where the 4 individual sub-matrices of **A** are presented in full detail by Eqs. (26)–(29), while the matrix **B** is given directly by (30)

$$\begin{bmatrix}\Delta\dot{\mathbf{x}}_1\\ \Delta\dot{\mathbf{x}}_2\end{bmatrix} = \begin{bmatrix}\mathbf{A}_{11} & \mathbf{A}_{12}\\ \mathbf{A}_{21} & \mathbf{A}_{22}\end{bmatrix}\cdot\begin{bmatrix}\Delta\mathbf{x}_1\\ \Delta\mathbf{x}_2\end{bmatrix} + \mathbf{B}\cdot\Delta\mathbf{u} \tag{25}$$

$$\mathbf{A}_{11} = \begin{bmatrix}
0 & \omega_b\omega_{VSM,0} & \frac{\omega_b}{c_f} & 0 & 0 & 0 & -\frac{\omega_b}{c_f} & 0 & 0 & 0\\
-\omega_b\omega_{VSM,0} & 0 & 0 & \frac{\omega_b}{c_f} & 0 & 0 & 0 & -\frac{\omega_b}{c_f} & 0 & 0\\
\frac{\omega_b\left(k_{ffv}-1-k_{AD}-k_{pc}k_{pv}\right)}{l_f} & -\frac{\omega_b c_f k_{pc}\omega_{VSM,0}}{l_f} & -\frac{\omega_b\left(k_{pc}+r_f\right)}{l_f} & 0 & \frac{\omega_b k_{ic}}{l_f} & 0 & \frac{\omega_b k_{pc}\left(k_{ffi}-k_{pv}r_v\right)}{l_f} & \frac{\omega_b k_{pc}k_{pv}l_v\omega_{VSM,0}}{l_f} & -\frac{\omega_b k_{AD}}{l_f} & 0\\
\frac{\omega_b c_f k_{pc}\omega_{VSM,0}}{l_f} & \frac{\omega_b\left(k_{ffv}-1-k_{AD}-k_{pc}k_{pv}\right)}{l_f} & 0 & -\frac{\omega_b\left(k_{pc}+r_f\right)}{l_f} & 0 & \frac{\omega_b k_{ic}}{l_f} & -\frac{\omega_b k_{pc}k_{pv}l_v\omega_{VSM,0}}{l_f} & \frac{\omega_b k_{pc}\left(k_{ffi}-k_{pv}r_v\right)}{l_f} & 0 & -\frac{\omega_b k_{AD}}{l_f}\\
-k_{pv} & -c_f\omega_{VSM,0} & -1 & 0 & 0 & 0 & k_{ffi}-k_{pv}r_v & k_{pv}l_v\omega_{VSM,0} & 0 & 0\\
c_f\omega_{VSM,0} & -k_{pv} & 0 & -1 & 0 & 0 & -k_{pv}l_v\omega_{VSM,0} & k_{ffi}-k_{pv}r_v & 0 & 0\\
\frac{\omega_b}{l_g} & 0 & 0 & 0 & 0 & 0 & -\frac{\omega_b r_g}{l_g} & \omega_b\omega_{VSM,0} & 0 & 0\\
0 & \frac{\omega_b}{l_g} & 0 & 0 & 0 & 0 & -\omega_b\omega_{VSM,0} & -\frac{\omega_b r_g}{l_g} & 0 & 0\\
-\omega_{AD} & 0 & 0 & 0 & 0 & 0 & 0 & 0 & -\omega_{AD} & 0\\
0 & -\omega_{AD} & 0 & 0 & 0 & 0 & 0 & 0 & 0 & -\omega_{AD}
\end{bmatrix} \tag{26}$$

$$\mathbf{A}_{12}=\begin{bmatrix}0&0&0&0&0&0&\omega_b v_{o,q,0}&0\\0&0&0&0&0&0&-\omega_b v_{o,d,0}&0\\0&0&0&\frac{\omega_b k_{iv}k_{pc}}{l_f}&0&\frac{\omega_b k_{pc}k_{pv}k_q}{l_f}&\frac{\omega_b\left(k_{pc}k_{pv}l_v i_{o,q,0}-c_f k_{pc}v_{o,q,0}\right)}{l_f}&0\\0&0&0&0&\frac{\omega_b k_{iv}k_{pc}}{l_f}&0&\frac{\omega_b\left(-k_{pc}k_{pv}l_v i_{o,d,0}+c_f k_{pc}v_{o,d,0}\right)}{l_f}&0\\0&0&0&k_{iv}&0&-k_{pv}k_q&k_{pv}l_v i_{o,q,0}-c_f v_{o,q,0}&0\\0&0&0&0&k_{iv}&0&-k_{pv}l_v i_{o,d,0}+c_f v_{o,d,0}&0\\0&0&0&0&0&0&\omega_b i_{o,q,0}&0\\0&0&0&0&0&0&-\omega_b i_{o,d,0}&0\\0&0&0&0&0&0&0&0\\0&0&0&0&0&0&0&0\end{bmatrix} \tag{27}$$

$$\mathbf{A}_{21}=\begin{bmatrix}\omega_{LP,PLL}\cos(\delta\theta_{PLL,0})&\omega_{LP,PLL}\sin(\delta\theta_{PLL,0})&0&0&0&0&0&0&0&0\\-\omega_{LP,PLL}\sin(\delta\theta_{PLL,0})&\omega_{LP,PLL}\cos(\delta\theta_{PLL,0})&0&0&0&0&0&0&0&0\\0&0&0&0&0&0&0&0&0&0\\-1&0&0&0&0&0&-r_v&l_v\omega_{VSM,0}&0&0\\0&-1&0&0&0&0&-l_v\omega_{VSM,0}&-r_v&0&0\\-\omega_f i_{o,q,0}&\omega_f i_{o,d,0}&0&0&0&0&\omega_f v_{o,q,0}&-\omega_f v_{o,d,0}&0&0\\-\frac{i_{o,d,0}}{T_a}&-\frac{i_{o,q,0}}{T_a}&0&0&0&0&-\frac{v_{o,d,0}}{T_a}&-\frac{v_{o,q,0}}{T_a}&0&0\\0&0&0&0&0&0&0&0&0&0\end{bmatrix} \tag{28}$$

$$\mathbf{A}_{22}=\begin{bmatrix}-\omega_{LP,PLL}&0&0&0&0&0&0&\omega_{LP,PLL}\left(v_{o,q,0}\cos(\delta\theta_{PLL,0})-v_{o,d,0}\sin(\delta\theta_{PLL,0})\right)\\0&-\omega_{LP,PLL}&0&0&0&0&0&-\omega_{LP,PLL}\left(v_{o,d,0}\cos(\delta\theta_{PLL,0})+v_{o,q,0}\sin(\delta\theta_{PLL,0})\right)\\0&\frac{1}{v_{PLL,d,0}}&0&0&0&0&0&0\\0&0&0&0&0&0&k_q&l_v i_{o,q,0}\\0&0&0&0&0&0&-l_v i_{o,d,0}&0\\0&0&0&0&0&-\omega_f&0&0\\0&\frac{k_d k_{p,PLL}}{T_a v_{PLL,d,0}}&\frac{k_d k_{i,PLL}}{T_a}&0&0&0&-\frac{k_\omega}{T_a}&0\\0&\frac{\omega_b k_{p,PLL}}{v_{PLL,d,0}}&\omega_b k_{i,PLL}&0&0&0&0&0\end{bmatrix} \tag{29}$$

$$\mathbf{B}=\begin{bmatrix}0&0&0&0\\0&0&0&0\\0&\frac{\omega_b k_{pc}k_{pv}k_q}{l_f}&\frac{\omega_b k_{pc}k_{pv}}{l_f}&0\\0&0&0&0\\0&-k_{pv}k_q&k_{pv}&0\\0&0&0&0\\0&0&0&0\\0&0&0&0\\0&0&0&0\\0&0&0&0\\0&0&0&0\\0&0&0&0\\0&0&0&0\\0&0&0&0\\0&k_q&1&0\\0&0&0&0\\0&0&0&0\\\frac{1}{T_a}&0&0&\frac{k_\omega}{T_a}\\0&0&0&0\end{bmatrix} \tag{30}$$

References

[1] Beck H-P, Hesse R. Virtual synchronous machine. In: Proceedings of the 9th international conference on electrical power quality and utilisation, Barcelona (Spain); 9–11 October 2007. 6 pp.

[2] Driesen J, Visscher K. Virtual synchronous generators. In: Proceedings of the IEEE power and energy society 2008 general meeting: conversion and delivery of energy in the 21st century, Pittsburgh (PA, USA); 20–24 July 2008. 3 pp.

[3] Zhong Q-C, Weiss G. Synchronverters: inverters that mimic synchronous generators. IEEE Trans Indust Electron 2011;58(4):1259–67.

[4] D'Arco S, Suul JA. Virtual synchronous machines – classification of implementations and analysis of equivalence to droop controllers for microgrids. In: Proceedings of IEEE PowerTech Grenoble 2013, Grenoble (France); 16–20 June 2013. 7 pp.

[5] Visscher K, De Haan SWH. Virtual synchronous machines (VSG's) for frequency stabilization in future grids with a significant share of decentralized generation. In: Proceedings of the CIRED seminar 2008: SmartGrids for distribution, Frankfurt (Germany); 23–24 June 2008. 4 pp.

[6] Sakimoto K, Miura Y, Ise T. Stabilization of a power system with a distributed generator by a virtual synchronous generator function. In: Proceedings of the 8th international conference on power electronics – ECCE Asia, Jeju (Korea); 30 May–3 June 2011. 8 pp.

[7] Hesse R, Turschner D, Beck H-P. Micro grid stabilization using the virtual synchronous machine (VISMA). In: Proceedings of the international conference on renewable energies and power quality, ICREPQ'09, Valencia (Spain); 15–17 April 2009. 6 pp.

[8] Chen Y, Hesse R, Turschner D, Beck H-P. Dynamic properties of the virtual synchronous machine (VSIMA). In: Proceedings of the international conference on renewable energies and power quality, ICREPQ'11, Las Palmas (Spain); 13–15 April 2011. 5 pp.

[9] Chen Y, Hesse R, Turschner D, Beck H-P. Investigation of the virtual synchronous machine in the island mode. In: Proceedings of the 2012 3rd IEEE innovative smart grid technologies Europe conference, Berlin (Germany); 15–17 October 2012. 6 pp.

[10] Bevrani H, Ise T, Miura Y. Virtual synchronous generators: a survey and new perspectives. Int J Electr Power Energy Syst 2014;54:244–54.

[11] D'Arco S, Suul JA, Fosso OB. Control system tuning and stability analysis of virtual synchronous machines. In: Proceedings of the 2013 IEEE energy conversion congress and exposition, ECCE 2013, Denver (CO, USA); 15–19 September 2013. p. 2664–71.

[12] Pogaku N, Prodanović M, Green TC. Modeling, analysis and testing of autonomous operation of an inverter-based microgrid. IEEE Trans Power Electron 2007;22(2):613–25.
[13] Rocabert J, Luna A, Blaabjerg F, Rodríguez P. Control of power converters in AC microgrids. IEEE Trans Power Electron 2012;27(11):4734–49.
[14] D'Arco S, Suul JA, Fosso OB. Small-signal modeling and parametric sensitivity of a virtual synchronous machine. In: Proceedings of the 18th power systems computation conference, PSCC 2014, Wrocław (Poland); 18–22 August 2014. 9 pp.
[15] D'Arco S, Suul JA, Fosso OB. A Virtual Synchronous Machine Implementation for Distributed Control of Power Converters in SmartGrids. Electr Power Syst Res 2015;122:180–97.
[16] Machowski J, Bialek JW, Bumby JR. Power system dynamics and stability. Chichester (UK): Wiley; 1997 [chapters 2 and 5].
[17] Kaura V, Blasko V. Operation of a phase locked loop system under distorted utility conditions. IEEE Trans Indust Appl 1997;33(1):58–63.
[18] Kolstad H. Control of an adjustable speed hydro utilizing field programmable devices. Ph.D. thesis, Norwegian University of Science and Technology; 2002.
[19] Haddadi A, Joos G. Load sharing of autonomous distribution-level microgrids. In: Proceedings of the 2011 IEEE PES general meeting: the electrification of transportation and the grid of the future, Detroit (MI, USA); 24–28 July 2011. 9 pp.
[20] He J, Li YW. Design, and implementation of virtual impedance for power electronics interfaced distributed generation. IEEE Trans Indust Appl 2011;47(6):2525–38.
[21] Mo O, Hernes M, Ljøkelsøy K. Active damping of oscillations in LC-filter for line connected, current controlled, PWM voltage source converters. In: Proceedings of the 10th European conference on power electronics and applications, EPE 2003, Toulouse (France); 2–4 September 2003. 10 pp.
[22] Malinowski M, Kazmierkowski MP, Bernet S. New simple active damping of resonance in three-phase PWM converter with LCL filter. In: Proceedings of the 2005 IEEE international conference on industrial technology, ICIT 2005, Hong Kong; 14–17 December 2005. p. 861–5.
[23] Kroutikova N, Hernandez-Aramburo CA, Green TC. State-space model of grid-connected inverters under current control mode. IET Electr Power Appl 2007;1(3):329–38.
[24] Indu Rani B, Aravind CK, Saravana Ilango G, Nagamani C. A three phase PLL with a dynamic feed forward frequency estimator for synchronization of grid connected converters under wide frequency variations. Int J Electr Power Energy Syst 2012;41(1):63–70.
[25] Golestan S, Ramezani M, Guerrero JM. An analysis of the PLLs with secondary control path. IEEE Trans Indust Electron 2014;61(9):4824–8.
[26] Kundur P. Power system stability and control. New York: McGraw-Hill; 1994.
[27] Blasko V, Kaura V. A New mathematical model and control of a three-phase AC–DC voltage source converter. IEEE Trans Power Electron 1997;12(1):116–23.
[28] Garofalo F, Iannelli L, Vasca F. Participation factors and their connections to residues and relative gain array. In: Proceedings of the 15th triennal world congress of the international federation of automatic control, Barcelona (Spain); 21–26 July 2002. 6 pp.
[29] D'Arco S, Suul JA, Fosso OB. Automatic tuning of cascaded controllers for power converters using eigenvalue parametric sensitivities. IEEE Trans Indust Appl 2015;51(2):11.